Spinodal decomposition as a possible void initialization mechanism for spallation in shock melted materials under high strain rates

Yutong Yang ⬤,[1] Zixiang Yan ⬤,[2] Hao Liu ⬤,[3] Jingxiang Shen ⬤,[4,5,*] and Wei Kang ⬤[5,†]

[1]*HEDPS, Center for Applied Physics and Technology and School of Physics, Peking University, Beijing 100871, China*
[2]*School of Science, Beijing University of Posts and Telecommunications, Beijing 100876, China*
[3]*Department of Applied Physics, School of Physics and Electronics, Hunan University, Changsha 410082, China*
[4]*Institute of Applied Physics and Computational Mathematics, Beijing 100094, China*
[5]*HEDPS, Center for Applied Physics and Technology, College of Engineering, Peking University, Beijing 100871, China*

We show with molecular dynamics simulations that spinodal decomposition is a probable initiation mechanism of spallation in impact-melted samples at extremely high strain rates. The formation of voids or bubbles is a secondary process following the spinodal amplification of density fluctuations. As a result, the spallation strength can be related to the inherent thermodynamic property of the liquid, i.e., the liquid-gas spinodal curve, which can be determined by independent equation-of-state studies in prior. This connection between high strain-rate spallation and spinodal decomposition may be further examined in future experiments.

I. INTRODUCTION

Dynamic spallation processes of materials at high strain rates are of critical importance to a wide range of scientific and engineering disciplines, including astrophysics, material sciences, and aerospace engineering [1–4]. It is involved in subjects like planetary collisions [5], jet engine debris impacts [6], and laser-driven impact experiments [7].

Typically, spallation occurs when a strong shock wave interacts with a free surface. For decaying shocks generated by impacts, the returning rarefaction waves generated when shock breaks out of the free surface would superimpose with the decaying part of the shock following the shock front. Strong tensile stress can be created, which may break the material from inside at this stretched zone. Depending on the strength and rate of stretching, material may fail in a complicated way, which is not yet fully understood.

The formation of voids is considered one of the main causes for spallation [8–10]. However, for different impact strength and strain rates, there are fundamental differences between void formation mechanisms. For relatively weak impacts and relatively low strain rates, most of the bulk material would remain solid during spallation. The formation of voids in these cases is generally described within the framework of solid mechanics [11,12]: Voids are initiated from imperfections (like impurities, vacancies, dislocations, grain boundaries, and cracks) and may grow by vacancy diffusion and plastic flow [13,14] before causing failure.

On the other hand, owing to the recent development of high-power short-pulse lasers and advanced x-ray diagnostic techniques, spallation induced by much stronger impacts

can be realized and probed *in situ* [1,15,16]. With strong impact, the bulk material may have crossed the liquid-solid phase boundary upon the arrival of the forward-propagating shock front, i.e., becoming liquid before encountering the tensile stress. This eliminates the possibility of void formation around imperfections in bulk solid materials. Also, short-pulse impacts are naturally accompanied by very high strain rates (up to 10^9 s^{-1} [1]). This kind of microspalling in liquids shows distinct phenomena both in simulations [17,18] and experiments [19–21]. Detailed knowledge concerning the mechanism for spallation under such extreme conditions remains unclear.

Molecular dynamics (MD) investigations have previously shown [1,22,23] that, when the liquid phase is involved in spallation, bubblelike voids of nearly spherical shape can be observed, which is usually regarded as a signal of classical nucleation in metastable (overheated) liquids. On the other hand, however, it has also been long conjectured that spinodal decomposition, i.e., phase separation in the unstable zone of the liquid-gas phase diagram, could be the dominating mechanism of void formation at high strain rates [3,21,24,25].

Note that these two kinds of initiating mechanisms are physically distinct. The former implies a strong dependence on kinetic features, such as the nucleation rate, while the latter indicates that thermodynamic features should be dominant for spallation under such extreme conditions. Therefore, for both physical understanding and application purposes, it is of considerable interest to identify how the generation of voids is triggered in such extreme conditions.

In this paper, we show with MD simulations that, for shock-melted material at high enough strain rates, spallation originates from spinodal decomposition. Evidence for spinodal decomposition, like the static structural factor in the stretched region prior to void formation, is presented and discussed. As a result, the spallation strength can be further

---
*Contact author: shenjingxiang93@163.com
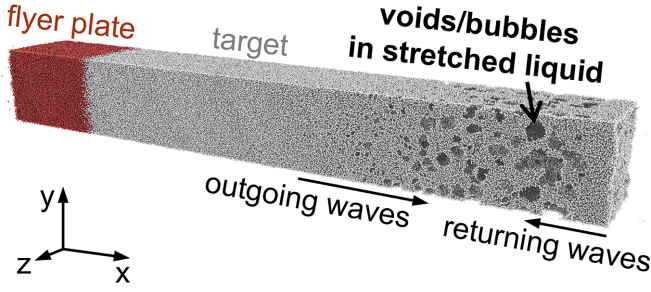†Contact author: weikang@pku.edu.cn

FIG. 1. An illustration of our molecular dynamics (MD) simulations for spallation. The initial dimension of the target is $81 \times 18.225 \times 18.225$ nm. The impact by the flyer plate is strong enough to melt the aluminum target at the shock front. Then, the voids/bubbles form and grow in liquid aluminum, thus taking spherical shapes due to surface tension.

related to the liquid-gas spinodal boundary: In this high strain-rate regime, spallation strength obtained for several different shock strengths and strain rates can be collapsed to a single curve related to the spinodal curve, indicating that the kinetic details of the dynamical impact process are largely irrelevant under these extreme conditions.

The remaining parts of this paper are organized as follows. In Sec. II, we describe numerical details for the MD simulation of spallation as well as our methods for determining the spinodal and binodal (equilibrium phase boundary) curves. Our main simulation results and the signatures for spinodal decomposition are analyzed and discussed in Sec. III. This paper concludes in Sec. IV with a short summary.

II. METHODOLOGY AND NUMERICAL DATA

A. MD simulation of spallation induced by flyer plate impact

Spallation in this paper is generated by flyer plate impact in planar geometry [2,26]. This process is simulated by nonequilibrium MD so that the initial stage of void formation can be captured with atomic resolution, as schematically displayed in Fig. 1.

Here, aluminum is taken as an example, of which both the flyer plate and the planar target in our simulations are made. The interactions among the aluminum atoms are described by the modified embedded-atom method (MEAM) empirical potential, which was developed by Aitken *et al.* [27] and improved by Yan *et al.* [28]. It was shown in previous studies that this empirical potential has a good description of lattice constant, cohesive energy, and dissociation energy, along with other mechanical and thermodynamic properties of aluminum. We have also checked its validity for the liquid phase by comparing the critical point and radial distribution function predicted by this potential against experimental and ab initio results [29–31].

The collision velocity v_c between the flyer plate and the target is set high enough to ensure melting of the aluminum sample upon the forward passage of the shock, and subsequent stretching of the sample due to rarefaction waves would lead to void and spallation in this liquid.

To be specific, periodic boundary conditions are enforced in y and z directions of the simulation system, whereas free

boundary conditions are applied in the x direction along which impact is applied (Fig. 1). The target is an 81-nm-thick aluminum slab with 18.225×18.225 nm lateral intersection and a lattice constant of 0.405 nm, containing 1.62 million atoms. The [100] crystalline direction is aligned with the x axis. Since the aluminum samples are ensured to be shock melted, the crystalline direction for loading/unloading would have no influence on spallation behavior.

At initialization, the flyer plate and the sample are separated from each other by a small distance of 3 nm. Both are equilibrated for 20 ps at 300 K. Then the thermal reservoir is turned off, and the flyer plate and target are assigned with bulk velocities $\pm v_c$ along the x axis in opposite directions to generate impact. The shock processes were carried out under the NVE ensemble to ensure the conservation of energy in the system. In this paper, we use flyer plates with thicknesses ranging from 10.125 to 40.5 nm, creating decaying shocks with different decay rates. Here, v_c is adjusted between 4 and 10 km/s to give relative impact velocities ranging from 8 to 20 km/s, large enough to ensure shock melting.

After collision, two strong shocks are launched from the impact plane and propagate along $\pm x$ directions in the target and the flyer plate. Because the flyer plate is much thinner than the target, the right-going shock propagating in the target will soon become a decaying shock, with rarefaction waves following the shock front. When the shock front reaches the free surface on the right end of the target, returning rarefaction waves are generated at the free surface and propagate along the $-x$ axis. These two groups of rarefaction waves interact with each other, generating negative pressure and hence voids and bubbles, finally leading to spallation (Fig. 1).

All simulations are carried out using the open-source software LAMMPS [32], and the simulation time step in this study is set to 1 fs.

B. Determining the binodal and spinodal curves

Since we would like to demonstrate that the liquid aluminum sample undergoes spinodal decomposition when these voids and/or bubbles are initiated, we calculate the liquid-gas binodal and spinodal curves for our aluminum system characterized by this MEAM potential [28].

The binodal curve refers to the liquid-gas phase equilibrium curve, i.e., the boundary dividing pure phases from the coexistence zone. The spinodal curve is a second boundary inside the coexistence zone, dividing the metastable region of the homogeneous phase against the absolutely unstable one [33,34].

The binodal curve is determined by a direct MD simulation of a liquid-gas coexisting system [35,36]. The simulation box is $56.2 \times 16.2 \times 16.2$ nm, with periodic boundary conditions applied in all three directions. At initialization, a liquid slab pre-equilibrated at temperature above the melting point is defined which occupies $\frac{1}{3.5}$ of the total volume. The remaining part of the simulation box is left as vacuum. Then the system undergoes NVT evolution for 500 ps at a given temperature T to reach equilibrium. After that, further 100 ps NVT trajectories are averaged to obtain densities of the liquid and phases at this temperature T [yellow squares and blue triangles in Fig. 2(a)]. We see that, <3000 K, the equilibrium density of
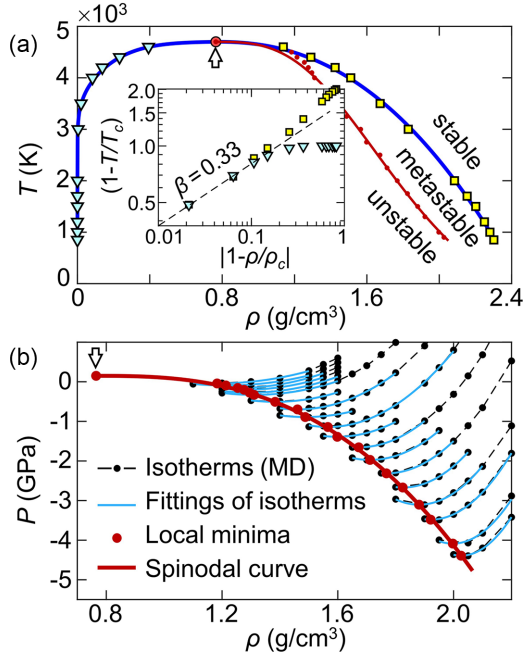
FIG. 2. The binodal and spinodal curves of this liquid-gas aluminum system. (a) The temperature-density phase diagram. The square and triangle markers are the results of phase-equilibrium simulations at different temperatures. A fitting of the binodal (co-existence) curve is shown in blue. The critical point, marked by the arrowhead, is located to satisfy $T - T_c \propto |\rho - \rho_c|^{0.33}$ (inset). The high-density branch of the spinodal curve is presented in red, which is determined following the steps shown in panel (b). (b) The spinodal curve was determined from molecular dynamics (MD) simulations of metastable isotherms. Black: Isotherms between 900 and 4500 K. Blue curves: Parabolic fittings to these isotherms near the local minima. Red dots: Local minima of the fittings. The pressure-density spinodal curve is then obtained by fitting these red dots (solid red curve).

the gas phase effectively becomes zero, so bubbles under these conditions are voids.

We use the $T(\rho)$ binodal curve to determine the critical point (ρ_c, T_c). The values of ρ_c and T_c are adjusted so that the binodal curve satisfies $T - T_c \propto |\rho - \rho_c|^\beta$ near the critical point with the critical exponent following the Ising universality class $\beta \approx 0.33$ [37]. The resulting T_c is 4700 K, and ρ_c is 0.765 g/cm^3. Pressure at the critical point can be estimated in a similar manner as $P_c = 0.15$ GPa, in accordance with existing experiments [29,30].

The spinodal curve is defined as $(\partial p / \partial \rho)_T = 0$ along isotherms of the homogeneous system [38]. Here, only the high-density branch, which separates the unstable zone from metastable liquid, is relevant to this paper. With regular equilibrium MD simulations, isotherms approaching $(\partial p / \partial \rho)_T = 0$ are not directly accessible since the state of matter involved here is certainly out of equilibrium. The system is absolutely unstable on one side and metastable on the other side. On the absolutely unstable side, it is very unlikely to conduct simulations of the pure phase of any kind because, in the $(\partial p / \partial \rho)_T < 0$ region, phase separation occurs immediately without any energy barrier. Fortunately, the homogeneous

phase can be accessed by MD simulation on the metastable side if nucleation does not occur. We therefore follow Guissani and Guillot [39,40], using a small system ($N = 108$) in the MD simulations to suppress long-wavelength fluctuations and delay the phase separation in the metastable liquid phase. In our simulations, each state point was relaxed for 500 ps under the NVT ensemble, during which period nucleation does not occur. This time period is enough for the system to relax on the atomic scale. The time average of the last 100 ps of this 500 ps trajectory is taken to calculate thermodynamic quantities of the metastable state. In this way, the isotherm can be obtained in the metastable zone, so that the local minima $(\partial p / \partial \rho)_T = 0$ can be approached from the metastable side. As revealed previously, this method can determine the equation of state near the spinodal curve from the metastable side with satisfactory precision.

The isotherms obtained in this way are smoothed by performing parabolic fittings near their local minima, and we take the minima of these fittings as the $(\partial p / \partial \rho)_T = 0$ points. In this way, we obtain the pressure, density, and temperature values of these data points on the spinodal curve. A fitting to these points (starting from the critical point with zero slope) thus gives our estimation of the spinodal curve.

Note that, while the phase coexistence (binodal) curve always has positive pressure for the liquid-gas system, the spinodal curve goes to negative pressures. This is exactly where spallation starts, as will be shown below.

III. RESULTS AND DISCUSSION

In this section, evidence for spinodal decomposition in the initiating phase of spallation is provided from different angles, and then the relation between spallation strength and the spinodal curve is discussed.

A. Dynamics of spallation and formation of voids

In Fig. 3, the case with collision velocity $v_c = 5$ km/s and the 10.125-nm-thick flyer plate is studied in detail, with special attention paid to the period and region where voids are initiated.

Figure 3(a) shows the pressure profiles at four selected time moments $t = 1.4, 1.8, 2.2,$ and 2.6 ps after shock breaks out from the free surface. The horizontal dashed black line represents zero pressure. We have added a -10 GPa shift between adjacent profiles for better visualization. The stretched region behind the free surface with negative pressure is clearly visible. The region of material in which voids are first going to initiate is traced through these time points, as marked by the shaded blue area.

Time evolution of density and pressure in this "most unstable region" traced through many time steps are shown in Fig. 3(b), together with the $P(\rho)$ spinodal curve. It is clear that only after the state of matter enters the unstable "spinodal" zone that the tensile stress begins to release due to phase separation.

Nevertheless, Figs. 3(a) and 3(b) suggest that the system crosses the spinodal boundary just before the time point marked by blue, i.e., 1.8 ps after shock breakout. We can take a close look at the MD sample in the vicinity of this time point.
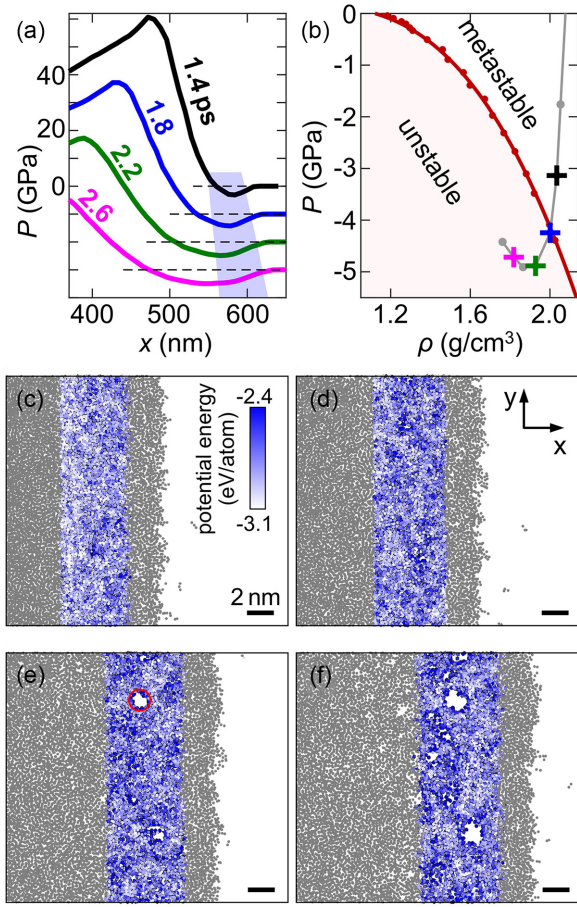
FIG. 3. Time evolution of the spalling shock-melted liquid before and after void/bubble formation. (a) The pressure profiles at 1.4, 1.8, 2.2, and 2.6 ps after shock breaking out from the free surface. The stretched region where voids first appear is traced through time and marked by the shaded blue region. We have added a -10 GPa shift between the profiles of adjacent time points for better visualization. Dashed black lines represent zero pressure. (b) The pressure-density trajectory for the traced stretched region. The spinodal curve calculated in Fig. 2(b) is shown as a reference. The black, blue, green, and magenta crosses correspond to 1.4, 1.8, 2.2, and 2.6 ps after shock breaks out. Note that the horizontal axis represents the nominal density, i.e., the average density, including the volume of voids. It decreases monotonically as voids grow during stretching. While density for the pure liquid phase should increase slightly once tensile stress starts to release. (c)–(f) Atomic configurations near the free surface at 1.4, 1.8, 2.2, and 2.6 ps after shock breaks out. We take a 1.0-nm-thick slice in the z direction. The region that is traced and analyzed above is colored in white-blue according to the local potential energy (which serves as a representation of density). Here, voids initiate in the third snapshot [panel (e)], and we mark a typical void with a near spherical shape with the red circle.

The atomic configurations for a slice in the x-y plane with a thickness of 1.0 nm centered around $z = 14.0$ nm is shown in Figs. 3(c)–3(f). These four panels correspond to the above selected moments: $t = 1.4, 1.8, 2.2,$ and 2.6 ps after shock breakout, respectively. The selected most unstable region mentioned above is colored in white-blue according to the local per-atom potential energy. Note that, in the stretched region, potential energy between atoms correlates negatively with density; thus, lower density regions appear in darker blue.

Before crossing the spinodal curve, as shown in Figs. 3(c) and 3(d), it is important to note that there is no sign of voids or bubbles in this early stage of stretching. Instead, in Fig. 3(d), there are floclike patterns [41,42] of density modulations, of which the characteristic wavelength is ~2 nm, as estimated by the average distance between low-density regions. This kind of pattern is a typical feature of spinodal decomposition [43,44]. Therefore, it seems that spinodal decomposition starts as soon as the system enters the unstable zone. This kind of matching is quite interesting since the observation of floclike density modulation in the direct MD simulation of dynamic spallation is methodologically independent of the calculation of spinodal boundary derived from our metastable equation-of-state simulations.

Then the release of tensile pressure begins as soon as void appears. When voids are generated, the volume occupied by the liquid phase decreases, and so does the average distance between atoms in the liquid phase, which reduces the stretching as well as the tensile forces between liquid atoms. Therefore, in this paper, the direct observation of voids in the atomic configuration [Fig. 3(e), red circle] and the release of tensile pressure [the green cross in Fig. 3(b)] are regarded as two criteria for the initiation of void. With these two criteria, it is clear that, for shock-melted systems at such high strain rates, the void formation starts in the unstable region, not in the metastable zone.

At first glance, it may be surprising to find that the void formation is initiated in the unstable region. With spinodal decomposition, the system would typically develop labyrinth patterns, as usually observed in alloy or solution systems [45]. This is quite different from the nearly spherical voids/bubbles observed here.

However, we would like to clarify that void formation is a secondary process following the spinodal decomposition process. Voids are initiated sometime later inside the unstable region, and the voids start to gain their spherical shapes only afterward during the nonlinear evolution stage due to the effects of surface tension. When the surface tension on the interfaces of the two phases is small, as typically in alloys and solutions, a full labyrinth structure will be developed. However, when the surface tension is strong enough, the nonlinear development of the spinodal decomposition will be dominated by the surface tension and near spherical voids or bubbles will be formed [46,47]. In short, such late-phase evolution of the void shape is physically different from how the voids are initiated, hence cannot be used to judge the initiating mechanism.

Therefore, the formation of voids or bubbles here is initiated by spinodal decomposition, not by classical nucleation.

There is an important difference between void formation triggered by spinodal decomposition and through classical nucleation. The classical nucleation mechanism involves a free energy barrier, and it takes some time to wait for this free energy barrier to be overcome by thermal fluctuations [48,49]. Therefore, if the liquid is stretched fast enough, i.e., the state of matter passes through the metastable zone of the phase diagram very fast, it will not have enough time for classical
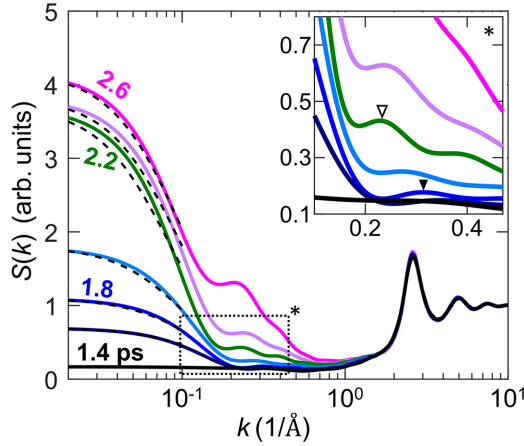
FIG. 4. Evolution of the structural factors $S(k)$ during stretching. Shown here are $S(k)$ at a total of seven time points: 1.4, 1.6, 1.8, 2.0, 2.2, 2.4, and 2.6 ps after shock breakout. Colors are consistent with Figs. 3(a) and 3(b). The long-wavelength (small k) peaks of $S(k)$ represent hydrodynamic fluctuations, which can be fitted by the typical Lorentzian profile (dashed black lines). The short-wavelength peaks and oscillations show the typical atomic-scale features of liquids. The spinodal peaks in the middle are marked by the dotted rectangle. Inset: A magnification of the dotted rectangle, with linear scales on both axes.

nucleation to occur. As a result, the liquid would be quenched deeply into the unstable region.

On the other hand, once entering the unstable spinodal region, the free energy barrier for creating density modulation diminishes. Thus, phase separation begins immediately after the state of matter crosses the spinodal curve. This mechanism should dominate under high enough strain rates.

B. Evolution of structure factor near the spinodal curve

In addition to the direct observation of the floclike density modulations, the onset of spinodal decomposition can be characterized in a more quantitative manner from the perspective of the (static) structure factor $S(\mathbf{k})$ [50,51]:

$$S(\mathbf{k}) = \langle |\tilde{n}(\mathbf{k})|^2 \rangle, \tag{1}$$

which is the Fourier transform of the density correlation function. Here, $\langle \cdot \rangle$ denotes the ensemble average, $\mathbf{k}$ is the wave number vector, and $\tilde{n}(\mathbf{k})$ is the Fourier transform of number density fluctuations $\tilde{n}(\mathbf{r}) = n(\mathbf{r}) - \bar{n}$ around the average density $\bar{n}$ in real space, namely,

$$\tilde{n}(\mathbf{k}) = \int d\mathbf{r} \exp(-i\mathbf{k} \cdot \mathbf{r})[n(\mathbf{r}) - \bar{n}]. \tag{2}$$

When a modulating structure with a characteristic length scale of l grows out of a homogeneous system, a peak centered around the corresponding characteristic wave number $k_s = 2\pi/l$ will appear and grow in the structure factor $S(k)$. For spinodal decomposition, $k_s \propto \sqrt{|(\partial P/\partial n)_T|}$ according to the Cahn-Hilliard theory [52,53]. Since the liquid-gas system here is rotational invariant, we have $S(\mathbf{k}) = S(k)$.

The $S(k)$'s along the time trajectory shown in Fig. 3(b) are plotted here in Fig. 4. They are calculated with atoms in a small region near the location of the largest tensile stress

to minimize the influence of density gradient along the x direction. Note that $S(k)$ displayed in Fig. 4 includes more snapshots along the trajectory in addition to those plotted in Figs. 3(c)–3(f).

On the long-wavelength side, $S(k)$ shows the signal for long-wavelength hydrodynamic density fluctuations [54,55], which is characterized as a Lorentzian peak centered at $k = 0$. On the short-wavelength side, the density correlation signals characterize the atomic-scale correlations between neighboring liquid atoms [56,57]. These atomistic features do not show any significant change along the time evolution trajectory even at the later stage of spallation when spherical voids/bubbles are present. This implies that the density as well as local atomic-scale structure in the liquid phase of the liquid-gas mixture do not change much, although the nominal/average density at the later stage is much lower than the liquid phase because of large low-density bubbles.

The characteristic peak of spinodal decomposition appears at the intermediate wave number between the hydrodynamic fluctuations and the atomic correlations [58]. In Fig. 4, this feature is spotted and marked by the dotted rectangle. This region of interest is zoomed-in as the inset of Fig. 4. It is clear that the spinodal peaks start to appear at $t = 1.8$ ps after shock breaking out from the free surface (solid arrowhead), but not for the previous time points. For some readers, it may be hard to tell by eye the difference between the patterns in Figs. 3(c) and 3(d), but here, the peak at $k \approx 0.3$ Å^{-1} appears at $t = 1.8$ ps but not at $t = 1.4$ ps, which serve as stronger evidence that these two time points are inherently different. This is consistent with Fig. 3(a) that spinodal decomposition begins only after entering the unstable zone of the phase diagram.

The center of the peak shifts gradually from $k \approx 0.3$ to 0.24 Å^{-1} within 0.4 ps (solid and empty arrowheads in Fig. 4, corresponding to a characteristic length $\sim$2.1–2.6 nm). This shift represents early stage coalescence of the density modulation patterns and is in line with the size change of the real-space patterns.

The peak in the spectrum of $S(k)$ corresponds to the presence of a spatially extended periodic density modulation structure in real space. Thus, the spinodal peak in $S(k)$ provides strong support for the existence of spinodal decomposition at the initial stage of spallation.

C. Spallation strength estimated from the spinodal curve

The spallation strength σ_s, i.e., the maximum tensile stress that the system is capable of resisting, is an important characteristic quantity in the study of spallation:

$$\sigma_s = \max_{x,t}\{|\sigma_x(x, t)|\}. \tag{3}$$

Here, σ_x represents the tensile stress in the direction of loading and release, but for liquids here, the stress is essentially isotropic.

Given that spallation is initiated by spinodal decomposition under the extreme conditions studied here, it is interesting to show that this insight can lead to a much simpler characterization of the spallation strength.

In previous studies, the spallation strength was usually given as an empirical scaling law with respect to spallation temperature and strain rate [2,59], but here, we would like

TABLE I. Flyer-plate thickness and collision velocity values for a total of 13 MD simulation cases. Their spallation strength and corresponding density and temperatures are show in Fig. 5.

Flyer-plate thickness H (nm)	Collision velocity v_c (km/s)
10.125	5, 6, 7, 8, 9, 10
20.25	4, 5, 6, 7
40.05	5, 6, 7

to show that the spallation strength for shock-melted samples under high enough strain rates can be associated with the spinodal curve, which relies only on the inherent thermodynamic property of the material.

To obtain the spallation strength *in situ*, we divide the simulation sample at each recorded time step into thin slices with a thickness of 1.2 nm along the x axis and record the average σ_x for each slice and time point. The maximum tensile stress in the simulation case can thus be obtained among all slices and time steps.

We have carried out a series of MD simulations using different flyer-plate thicknesses and collision velocities, as summarized in Table I. The spallation strength, along with the temperature and density values corresponding to the max-tensile-stress state, are recorded. As demonstrated in Fig. 5, these data points can all be collapsed onto a single curve close to the spinodal.

The spallation strength, when plotted as a function of density as in Fig. 5(a), turns out to show the same overall trend as the spinodal curve albeit with some quantitative deviations. Physically, the deviation is a reflection of the delayed observation of bubbles relative to spinodal decomposition. This discrepancy can be largely offset by introducing an *ad hoc* shift to density (dashed red curves):

$$\sigma_{\text{spallation}}(\rho) \approx P_{\text{spinodal}}(\rho - \Delta\rho); \tag{4a}$$

$$\sigma_{\text{spallation}}(T) \approx P_{\text{spinodal}}(T). \tag{4b}$$

The offset in density here in Fig. 5 is $\Delta\rho = 0.15$ g/cm^3. In a sense, this shift mimics the overshoot of the metastable liquid phase into the unstable zone as illustrated in Fig. 3(b).

In the physical sense, the overshoot of metastable liquid beyond the spinodal boundary would lead to a decrease in density, an increase in tensile stress, as well as a decrease in temperature. Thus, in principle, this *ad hoc* shift is needed for all three parameters T, P, and ρ. However, an interesting observation is that nearly no shift is needed for the spinodal curve to match the spallation data in the temperature-pressure coordinates. This is because the increase in tensile stress and the decrease in temperature would largely cancel each other: It just goes along the spinodal boundary itself, so the shift of the one-dimensional boundary becomes insignificant. As a result, only a shift in density is needed to give a fairly good correction [Eq. (4) and Fig. 5].

Instead of building phenomenological scaling laws for spallation strength from scratch, Eq. (4) offers a much simpler description using the spinodal boundary, although the relation of Eq. (4) is purely *ad hoc*, obtained using our MD simulations. It would remain valid if the sample is shock-melted
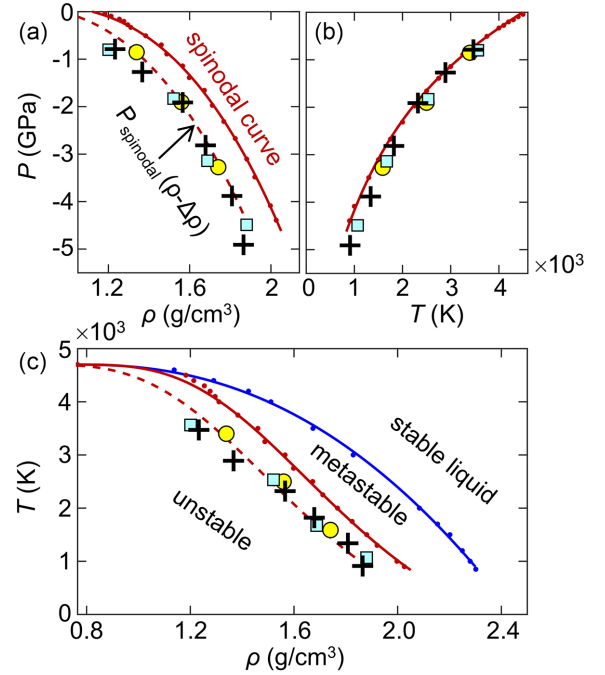

FIG. 5. The strength, density, and temperature at the onset of spallation can be related to the spinodal boundary. Results from 13 molecular dynamics (MD) simulations with different flyer-plate thicknesses H and collision velocities v_c are presented. Crosses: $H =$ 10.125 nm, $v_c =$ 5, 6, 7, 8, 9, and 10 km/s. Squares: $H = 20.25$ nm, v_c = 4, 5, 6, and 7 km/s. Circles: $H = 40.05$ nm, $v_c =$ 5, 6, and 7 km/s. This spallation boundary can be approximated by the spinodal curve (solid red curve) after a small *ad hoc* shift in the density axis (dashed red curve). Panels (a)–(c) show these results in the pressure-density, pressure-temperature, and temperature-density plots. The binodal phase boundary is also shown in the temperature-density plot for reference.

before spallation and that spinodal decomposition remains the dominant initiating mechanism of voids.

The value for $\Delta\rho$ should, of course, change with the exact condition for spallation if one wants to generalize this *ad hoc* law to a broader range of applications. Since $\Delta\rho$ reflects the delayed observation of bubbles relative to the initialization of spinodal decomposition, it may be a function of strain rate. When the strain rate varies, the depth of the system penetrating the unstable region changes accordingly. This kind of generalization may relax the requirement on strain rates for the examination in future experiments or numerical studies.

IV. SUMMARY

In summary, we show with MD simulations that spinodal decomposition could be the primary initiation mechanism of spallation at extremely high strain rates. As a successive process, the nonlinear evolution of density modulation leads to void formation. This provides a mechanism of void formation without having to overcome any energy barrier and thus could be dominant under high strain rates.

By analyzing our MD simulation results on spallation, we provide evidence that the voids are initiated in the spinodal

zone: (1) The pressure and density values for the spalling layer under the maximum tensile stress have no doubt crossed the spinodal curve determined from independent equation-of-state simulations. (2) Density fluctuation shows flocklike patterns as well as spinodal peaks in the static structure factor $S(k)$ prior to the formation of voids. Also, the spallation strength for all our simulation cases with different flyer-plate thicknesses and impact velocities can be collapsed onto a single curve close to the spinodal boundary, which provides a better understanding of the behavior of spallation strength in this high strain-rate limit.

The proposed relation between spallation strength and spinodal decomposition curve may be further examined in future experiments.

[1] J. Coakley, A. Higginbotham, D. McGonegle, J. Ilavsky, T. D. Swinburne, J. S. Wark, K. M. Rahman, V. A. Vorontsov, D. Dye, T. J. Lane *et al.*, Sci. Adv. **6**, eabb4434 (2020).

[2] S.-N. Luo, Q. An, T. C. Germann, and L.-B. Han, J. Appl. Phys. **106**, 013502 (2009).

[3] F. Vidal, T. W. Johnston, J. C. Kieffer, and F. Martin, Phys. Rev. B **70**, 184125 (2004).

[4] E. N. Hahn, T. C. Germann, R. Ravelo, J. E. Hammerberg, and M. A. Meyers, Acta Mater. **126**, 313 (2017).

[5] E. P. Turtle and E. Pierazzo, Science **294**, 1326 (2001).

[6] M. Buyuk, S. Kan, and M. J. Loikkanen, J. Aerosp. Eng. **22**, 287 (2009).

[7] M. S. Krivokorytov, A. Y. Vinokhodov, Y. V. Sidelnikov, V. M. Krivtsun, V. O. Kompanets, A. A. Lash, K. N. Koshelev, and V. V. Medvedev, Phys. Rev. E **95**, 031101(R) (2017).

[8] L. Seaman, D. R. Curran, and D. A. Shockey, J. Appl. Phys. **47**, 4814 (1976).

[9] A. Strachan, T. Çağın, and W. A. Goddard III, Phys. Rev. B **63**, 060103(R) (2001).

[10] Q. Zhu, J. Shao, and P. Wang, Nanomater. **13**, 2308 (2023).

[11] J. N. Johnson, J. Appl. Phys. **52**, 2812 (1981).

[12] H. Sui, L. Yu, W. Liu, Y. Liu, Y. Cheng, and H. Duan, Matter Radiat. Extremes **7**, 018201 (2022).

[13] V. Dremov, A. Petrovtsev, P. Sapozhnikov, M. Smirnova, D. L. Preston, and M. A. Zocher, Phys. Rev. B **74**, 144110 (2006).

[14] A. M. Dongare, A. M. Rajendran, B. LaMattina, M. A. Zikry, and D. W. Brenner, Phys. Rev. B **80**, 104108 (2009).

[15] D. H. Kalantar, J. F. Belak, G. W. Collins, J. D. Colvin, H. M. Davies, J. H. Eggert, T. C. Germann, J. Hawreliak, B. L. Holian, K. Kadau *et al.*, Phys. Rev. Lett. **95**, 075502 (2005).

[16] J. A. Hawreliak, B. El-Dasher, H. Lorenzana, G. Kimminau, A. Higginbotham, B. Nagler, S. M. Vinko, W. J. Murphy, T. Whitcher, J. S. Wark *et al.*, Phys. Rev. B **83**, 144114 (2011).

[17] M. Xiang, H. Hu, and J. Chen, J. Appl. Phys. **113**, 144312 (2013).

[18] X.-X. Wang, A.-M. He, T.-T. Zhou, and P. Wang, Mech. Mater. **160**, 103991 (2021).

[19] T. D. Rességuier, L. Signor, A. Dragon, M. Boustie, G. Roy, and F. Llorca, J. Appl. Phys. **101**, 013506 (2007).

[20] J. Yang, X. Wang, L. Xu, Q. Wang, Y. Sun, J. Li, L. Zhang, Y. Li, Y. Yu, P. Wang *et al.*, Matter Radiat. Extremes **9**, 057803 (2024).

[21] M. B. Agranat, S. I. Anisimov, S. I. Ashitkov, V. V. Zhakhovskii, N. A. Inogamov, P. S. Komarov, A. V. Ovchin-nikov, V. E. Fortov, V. A. Khokhlov, and V. V. Shepelev, JETP Lett. **91**, 471 (2010).

[22] K. Katagiri *et al.*, Phys. Rev. Lett. **126**, 175503 (2021).

[23] A. K. Upadhyay, N. A. Inogamov, B. Rethfeld, and H. M. Urbassek, Phys. Rev. B **78**, 045437 (2008).

[24] P. Lorazo, L. J. Lewis, and M. Meunier, Phys. Rev. Lett. **91**, 225502 (2003).

[25] S. I. Kudryashov, K. Lyon, and S. D. Allen, Phys. Rev. E **75**, 036313 (2007).

[26] B. Arman, S. N. Luo, T. C. Germann, and T. Cagin, Phys. Rev. B **81**, 144201 (2010).

[27] Z. H. Aitken, V. Sorkin, Z. G. Yu, S. Chen, Z. X. Wu, and Y. W. Zhang, Phys. Rev. B **103**, 094116 (2021).

[28] Z. X. Yan, C. Y. Zhang, X. Liu, Q. Miao, M. Fang, and W. Kang, Phys. Rev. B **106**, 174107 (2022).

[29] I. V. Lomonosov, Laser Part. Beams **25**, 567 (2007).

[30] P. Celliers and A. Ng, Phys. Rev. E **47**, 3547 (1993).

[31] N. Jakse and A. Pasturel, Sci. Rep. **3**, 3135 (2013).

[32] A. P. Thompson, H. M. Aktulga, R. Berger, D. S. Bolintineanu, W. M. Brown, P. S. Crozier, P. J. in 't Veld, A. Kohlmeyer, S. G. Moore, T. D. Nguyen *et al.*, Comput. Phys. Commun. **271**, 108171 (2022).

[33] P. D. Olmsted, W. C. K. Poon, T. C. B. McLeish, N. J. Terrill, and A. J. Ryan, Phys. Rev. Lett. **81**, 373 (1998).

[34] V. Testard, L. Berthier, and W. Kob, Phys. Rev. Lett. **106**, 125702 (2011).

[35] B. Xiao and L. Stixrude, Proc. Natl. Acad. Sci. USA **115**, 5371 (2018).

[36] J. Alejandre, D. J. Tildesley, and G. A. Chapela, J. Chem. Phys. **102**, 4574 (1995).

[37] H. Watanabe, N. Ito, and C.-K. Hu, J. Appl. Chem. Phys. **136**, 204102 (2012).

[38] S. Sastry, Phys. Rev. Lett. **85**, 590 (2000).

[39] Y. Guissani and B. Guillot, J. Chem. Phys. **98**, 8221 (1993).

[40] Y. Guissani and B. Guillot, J. Chem. Phys. **104**, 7633 (1996).

[41] M. B. Wise and P. C. Millett, Phys. Rev. E **98**, 022601 (2018).

[42] H. Tanaka and T. Sigehuzi, Phys. Rev. E **52**, 829 (1995).

[43] P. Perlekar, R. Benzi, H. J. H. Clercx, D. R. Nelson, and F. Toschi, Phys. Rev. Lett. **112**, 014502 (2014).

[44] A. Lamorgese and R. Mauri, Phys. Rev. E **94**, 022605 (2016).

[45] P. Das, P. K. Jaiswal, and S. Puri, Phys. Rev. E **102**, 012803 (2020).

[46] W. R. Osborn, E. Orlandini, M. R. Swift, J. M. Yeomans, and J. R. Banavar, Phys. Rev. Lett. **75**, 4031 (1995).

[47] E. D. Siggia, Phys. Rev. A **20**, 595 (1979).

[48] K. Binder, Phys. Rev. A **29**, 341 (1984).

[49] P. Bhimalapuram, S. Chakrabarty, and B. Bagchi, Phys. Rev. Lett. **98**, 206104 (2007).

[50] A. Chaudhri, J. B. Bell, A. L. Garcia, and A. Donev, Phys. Rev. E **90**, 033014 (2014).

[51] S. Delong, B. E. Griffith, E. Vanden-Eijnden, and A. Donev, Phys. Rev. E **87**, 033302 (2013).

[52] J. W. Cahn and J. E. Hilliard, J. Chem. Phys. **28**, 258 (1958).

[53] J. W. Cahn, Acta Metall. **9**, 795 (1961).

[54] P. Dutta and S. K. Sinha, Phys. Rev. Lett. **47**, 50 (1981).

[55] M. Lulli, L. Biferale, G. Falcucci, M. Sbragaglia, D. Yang, and X. Shan, Phys. Rev. E **109**, 045304 (2024).

[56] E. C. Svensson, V. F. Sears, A. D. B. Woods, and P. Martel, Phys. Rev. B **21**, 3638 (1980).

[57] L. Yelash, P. Virnau, W. Paul, K. Binder, and M. Müller, Phys. Rev. E **78**, 031801 (2008).

[58] K. Binder, C. Billotet, and P. Mirold, Z. Physik B **30**, 183 (1978).

[59] S. G. Srinivasan, M. I. Baskes, and G. J. Wagner, J. Appl. Phys. **101**, 043504 (2007).